

A thermally-coupled cascade free-piston Stirling engine-based cogeneration system

Yuanhang Chen^{a,b}, Guoyao Yu^{a,c,*}, Ying Ma^a, Jianhua Xue^a, Fawad Ahmed^{a,b}, Yangbin Cheng^a, Haojie Sun^{a,b}, Shunmin Zhu^{a,d}, Wei Dai^{a,b}, Ercang Luo^{a,b}

^a *Key Laboratory of Cryogenics, Technical Institute of Physics and Chemistry, Chinese Academy of Sciences, Beijing 100190, China*

^b *University of Chinese Academy Sciences, Beijing 100049, China*

^c *Institute of Optical Physics and Engineering Technology, Qilu Zhongke, Jinan 251000, China*

^d *Clean Energy Processes (CEP) Laboratory, Department of Chemical Engineering, Imperial College London, South Kensington Campus, London SW7 2AZ, UK*

* *Corresponding author: gyyu@mail.ipc.ac.cn (G. Yu)*

Abstract:

Resonant Stirling/thermoacoustic cycle engines show great potential in efficiently recovering waste heat in small- or micro-scale applications. However, there is a significant research gap regarding the development of resonant Stirling/thermoacoustic cycle engines capable of effectively harnessing variable-temperature heat sources through cascade utilization. In this paper, a cogeneration system was proposed based on a thermally-coupled cascade dual-opposed free-piston Stirling engine. Through a multi-stage arrangement, the prototype enhances overall exergy efficiency by scavenging different grade heat. According to test results, with an input heating power of 20 kW for each stage, the corresponding heating temperatures for the three stages were 418.7 °C, 348.2 °C, and 302.8 °C, respectively. The demonstration setup provided simultaneous thermal power of 44.72 kW and electric power of 10.18 kW, resulting in an overall thermal-to-electric efficiency of 16.48% and an overall combined heat and power efficiency of 88.87%. Theoretically, compared with a single-stage system, the exergy efficiency improved from 36.3% to 43.9%, representing a relative improvement of more than 20%. This study provides valuable insights into the operating characteristics of multi-stage free-piston Stirling engine-based cogeneration systems and contributes to the development of waste heat recovery systems.

Keywords

energy conversion, free-piston Stirling generator, multi-stage system, combined heat and power, thermoacoustic

N.B.: This is the accepted version of this article. The published version of the article can be found at: <https://doi.org/10.1016/j.applthermaleng.2023.121679>

Nomenclature		T_{w-out}	temperature of circulating water at outlet of system (K)
		$T_{w-out,i}$	temperature of circulating water at outlet of i th AHX (K)
Symbols		U	volume flow rate ($m^3 s^{-1}$)
A_p	cross-sectional area of the power piston (m^2)	U_p	the volume flow rate of the power piston ($m^3 s^{-1}$)
C	electric capacitance of the linear alternator (F)	v	velocity of a moving part ($m s^{-1}$)
c_p	specific heat ($J kg^{-1} K^{-1}$)	W_a	acoustic power (W)
E_i	i th stage utilized exergy (W)	W_e	output electric power of system (W)
E_{max}	maximize exergy contained in the input heat (W)	$W_{e,i}$	output electric power of the i th stage FPSG (W)
E_{actual}	total actual utilized exergy (W)	X_{amp}	displacement amplitude of a moving part (m)
E_{total}	total exergy contained in the heat carrier (W)	Z	acoustic impedance ($Pa s m^{-3}$)
I	current of the linear alternator (A)	Z_{engine}	acoustic impedance of FPSE ($Pa s m^{-3}$)
K_p	spring stiffness of power piston ($N m^{-1}$)	Z_{LA}	acoustic impedance of Linear alternator ($Pa s m^{-3}$)
L	electric inductance of the linear alternator (H)	ΔT	single-stage temperature difference (K)
M	mass of the power piston (kg)	η_{CHP}	overall efficiency
\dot{m}	mass flow rate of heat carrier ($kg s^{-1}$)	η_{max}	maximal efficiency of exergy utilization
n	total stage number of the cogeneration system	η_{LA}	acoustic-to-electric efficiency
p_{comp}	pressure wave amplitude in the compression space (Pa)	η_{rel}	relative efficiency of exergy utilization
p	pressure wave (Pa)	η_{t-e}	thermal to electric efficiency
Q_c	heat rejected at the AHX (W)	η_{total}	total efficiency of exergy utilization
Q_{coil}	joule heat generation by coil (W)	ω	angular frequency (s^{-1})
Q_{damp}	heat caused by mechanical resistance (W)	θ_{pU}	phase difference of pressure and volume flow rate ($^\circ$)
Q_{in}	gross input heating power of system (W)	τ	force factor ($N A^{-1}$)
Q_{in-num}	actual heating power entering the engine (W)	Mathematical codes	
$Q_{in,i}$	gross input heating power of the i th stage dual-opposed FPSG (W)	i	$\sqrt{-1}$, imaginary unit
Q_w	gross rejected heat of system (W)		

$Q_{w,i}$	gross rejected heat of the i th-stage dual-opposed FPSG (W)	Im()	imaginary part of
R_{in}	coil resistance (Ω)	Re()	real part of
R_m	mechanical damping coefficient ($N s m^{-1}$)		magnitude of the complex number
R_{mp}	mechanical damping coefficient of the power piston ($N s m^{-1}$)	^	complex variable
R_{out}	external load resistance (Ω)	Abbreviation	
T	temperature (K)	AHX	ambient heat exchanger
T_0	ambient temperature (K)	CHP	combined heat and power
T_h	HHX wall temperature (K)	Exp	experiment
T_{h-in}	temperature of heat carrier at inlet (K)	FPSE	free-piston Stirling engine
T_{h-out}	temperature of heat carrier at outlet (K)	FPSG	free-piston Stirling generator
T_i	temperature of the i th stage HHX (K)	HHX	hot heat exchanger
T_{w-in}	temperature of circulating water at inlet of system (K)	LA	linear alternator
$T_{w-in,i}$	temperature of circulating water at inlet of i th AHX (K)	Sim	simulation

1. Introduction

The exponential growth in population and the improvement in quality of life have inevitably resulted in a surge in energy consumption, thereby giving rise to various challenges such as global climate change, air pollution, and energy scarcity. From the perspective of energy producers, there are generally two primary approaches to address these issues. The first approach involves the development and advancement of renewable energy sources including solar power, wind energy, biomass utilization, and geothermal resources. The second approach focuses on enhancing the efficiency and performance of energy conversion systems [1].

According to reports, a substantial amount of thermal energy is directly released into the environment, constituting over 50% of global energy consumption [1]. Recovering waste heat, which involves capturing, transferring, and harnessing waste heat to generate desired thermal energy or produce electricity and mechanical power, holds significant potential for addressing the current energy predicament [2].

The quality of waste heat sources can generally be classified into low (below 230 °C), medium (230–650 °C), and high (above 650 °C) grades based on their temperature levels [3]. After decades of development, the utilization of high-temperature waste heat has been largely achieved; however, the recovery of abundant medium- and low-grade waste heat remains a formidable challenge. Numerous sources of medium-grade waste heat can be harnessed, including exhaust from internal combustion engines (ICEs), steam boiler exhaust, gas turbine exhaust, heat treating furnaces, drying and baking ovens, as well as cement kilns [3]. To date, numerous waste heat recovery methods have been developed, encompassing heat exchangers [4], heat pumps [5], thermodynamic cycles [6], direct electrical conversion devices (e.g., thermoelectric generation and thermal photovoltaic) [7], and thermomagnetic generator [8]. Among them, thermodynamic cycles, which efficiently convert waste heat into mechanical and/or electrical power, have garnered increasing attention in recent years. Prominent examples of such cycles include the conventional steam Rankine cycle [3], Organic Rankine Cycle (ORC) [6], Kalina cycle [9], and Stirling/thermoacoustic cycle [10,11].

The Rankine Cycle and Kalina cycle systems have demonstrated significant competitiveness in the context of waste heat recovery within the cement industry [9]. While such systems are most effective for large-scale heat utilization, traditional fossil fuel energy production systems remain prevalent in many industrial processes and small to medium-sized industries. As a promising solution for small- or micro-scale waste heat recovery, the Stirling/thermoacoustic cycle has garnered significant attention in recent decades due to its external combustion nature, operating flexibility across a wide temperature range, high theoretical thermal efficiency, and exceptional reliability [12,13]. Moreover, the Stirling/thermoacoustic cycle engines exhibit a relatively low onset temperature, rendering them highly suitable for harnessing medium- and low-grade waste heat [14,15].

Reputable studies have extensively employed Stirling/thermoacoustic technology for waste heat recovery. Robert [16] proposed the utilization of a thermoacoustic piezoelectric generator and chiller system for waste heat recovery from the exhaust of a heavy-duty truck's main diesel engine, resulting in the generation of 37 W electric power on a proof-of-concept prototype. In 2012, Li *et al.* [17] developed a beta-type kinematic Stirling engine prototype

driven by the exhaust gas from a gasoline engine for micro-CHP application, resulting in the generation of 3476 W of shaft power. Guven *et al.* [18] conducted a comparative analysis of alpha, beta, and gamma-type Stirling engines for waste heat recovery on a heavy-duty diesel engine. Their findings demonstrated that the Stirling engine with a beta-type configuration is more suitable for waste heat recovery applications due to its higher dimensionless power output and moderate pressure ratio achieved by such a configuration. The heat transfer between exhaust gas and working gas was investigated by Catapano *et al.* [19], who developed a prototype incorporating a Stirling engine, an ORC subsystem, and a latent thermal energy storage subsystem to recover waste heat from a ship's propulsion system [20]. The experimental results indicated that the net electrical energy generated by the Stirling engine accounted for 0.2% of the total fuel energy consumption. The authors proposed a thermoacoustic electric generator for the conversion of heat carried by vehicle exhaust into electric power [21]. A prototype of this thermoacoustic electric generator was constructed and tested using the exhaust stream from a hot gas test bench. The experimental results demonstrated a peak electrical power output of 570 W, corresponding to a maximum waste heat enthalpy-to-electrical energy conversion efficiency of 5% [22]. The standing-wave thermoacoustic engine developed by Mumith *et al.* [23] was designed for waste heat recovery from baking ovens in the biscuit manufacturing process. The potential of utilizing Stirling engine technology for numerical waste heat recovery applications in cement plants was demonstrated by Laazaar and Boutammachte [24]. Alali *et al.* [25] conducted a thermodynamic analysis on a hybrid system combining a Stirling engine and a double-effect absorption chiller, aiming to utilize waste heat from a gas turbine modular helium reactor. In summary, the recovery of waste heat by Stirling engines demonstrated the potential for generating practically useful levels of output power.

However, the heat capacity of the gaseous waste heat carrier is significantly limited, resulting in a substantial decrease in its temperature compared to that of a liquid counterpart for a given amount of heat transfer. Consequently, the waste heat scenario falls under the category of a variable-temperature heat source, inevitably leading to irreversible exergy loss. To ensure optimal performance of a Stirling/thermoacoustic cycle engine, its hot heat exchanger (HHX) must maintain a uniform temperature distribution; otherwise, localized streaming phenomena may occur and compromise the engine's efficiency. [10]. A significant reduction in the temperature of the waste heat carrier is inevitable [26], resulting in irreversible exergy loss and consequently limiting the rate of waste heat utilization. Conversely, a single-stage Stirling/thermoacoustic cycle engine lacks the capability to recover a majority of the waste heat due to its thermodynamic characteristics. To address these challenges, employing a multi-stage arrangement for the Stirling/thermoacoustic cycle engine could be considered an effective candidate to achieve sufficient waste heat utilization while maintaining a reasonable temperature drop across each engine.

In recent years, various multi-stage thermoacoustic engines capable of harnessing variable-temperature heat sources have been investigated for waste heat recovery purposes, including cascade arrangements [10,26], parallel arrangements [27], and looped arrangements [28]. In 2007, Luo *et al.* [29] proposed and patented a multi-stage thermoacoustic-Stirling hybrid engine comprising at least two parallel traveling wave loops and a shared resonator. Subsequently, Qiu *et al.* [30] proposed a thermoacoustic-Stirling hybrid engine featuring an

innovative regenerator capable of accommodating multi-temperature heat sources. Experimental investigations were conducted, and the findings substantiated the advantageous impact of this regenerator design on the engine's performance. In 2014, HEKYOM and its collaborators successfully developed a highly efficient thermoacoustic engine system featuring three cascade thermoacoustic amplification cells, accompanied by three recuperators and three loop heat pipes. This innovative system effectively harnesses waste heat from the exhaust gas of an ICE [10,31]. A similar cascade arrangement of a multi-stage thermoacoustic engine was also investigated by Nader *et al.* [26]. They conducted a comparative analysis of the performance of three different thermoacoustic engines (with one-, two-, and three-stage configurations, respectively) for waste heat recovery in extended-range hybrid electric vehicles. The findings revealed that the three-stage thermoacoustic engine with a cascade arrangement outperformed the other two configurations. In 2017, Bi *et al.* developed a three-stage looped traveling-wave thermoacoustic electric generator [28]. The findings revealed that compared to the thermoacoustic electric generator driven by a constant-temperature heat source, the output electrical power of the thermoacoustic electric generator experienced a significant decline when driven by a variable-temperature heat source; however, there was only a slight deterioration in thermal to electric efficiency [32]. Additionally, the same research group proposed a three-stage looped traveling-wave thermoacoustic engine system consisting of three parallel arrangement thermoacoustic engine units in each stage and also explored the feasibility of utilizing variable-temperature heat sources within this system [27].

The recovery of variable-temperature waste heat has predominantly relied on conventional thermoacoustic engines, which suffer from limitations such as intrinsic acoustic streaming, relevant losses, low exergy efficiency due to complete gas tuning, and low power density arising from lengthy resonators [33]. To address these drawbacks, a potential solution is to explore the use of a free-piston Stirling engine (FPSE) that utilizes a compact displacer for tuning while maintaining acoustic resonance. Unlike traditional kinematic Stirling engines, FPSEs offer extended lifespan and virtually maintenance-free operation by eliminating mechanical components like crankshafts and contact seals [34]. Recently, Jiang *et al.* proposed a multi-stage free-piston Stirling generator (FPSG) with bypass structures, specifically designed for variable-temperature waste heat recovery [35]. Simulation results showcased a notable 29.4% enhancement in thermal-to-electric efficiency compared to conventional single-stage FPSGs under similar heating conditions. Although these findings are promising, similar to many thermoacoustic engines, the amount of waste heat supplied to the thermoacoustic engine is restricted by the maximum length of Hot Heat Exchangers (HHXs) along the direction of wave propagation, resulting in a limited heat exchange interface [10]. The intricate mechanism behind such bypass structures remains inadequately understood, and experimental verification of this configuration is currently lacking.

To circumvent the dilemma, a novel multi-stage cogeneration system based on FPSE is proposed and developed in this study. The system integrates multiple independent FPSGs thermally to achieve a cascade utilization of variable-temperature heat sources. The stand-alone operation of each FPSG allows for unconstrained waste heat supply to the entire system, surpassing the limitations of thermoacoustic engines and multi-stage FPSGs with by-pass structures mentioned earlier. Furthermore, unlike double-acting FPSE [36] or multi-stage

looped traveling-wave thermoacoustic engines [28,37], the proposed system eliminates any inconsistencies. To the best of our knowledge, no previous work has reported on such a multi-stage FPSE-based cogeneration system. In this study, three key aspects warrant further investigation. Firstly, the viability of a numerical model based on a single-stage FPSG in predicting the performance of both dual-opposed and three-stage cogeneration systems remains uncertain. Secondly, the fabrication of a representative three-stage cogeneration system poses significant challenges to showcase its distinctive features. Lastly, addressing issues pertaining to prediction deviations and exploring their potential presents an intractable task.

In the subsequent sections, the theoretical analysis examines the significant advantages of the multi-stage system in comparison to the single-stage system. The numerical methodology employed in this study is introduced, followed by its validation on a single-stage dual-opposed free-piston Stirling generator (FPSG). Subsequently, a numerical investigation is conducted on a three-stage dual-opposed FPSG system using the validated numerical methodology. To assess the combined heat and power (CHP) performance, a demonstration setup of the system is constructed and subjected to rigorous testing. By comparing results obtained from calculations and experiments, insights are gained into improving the performance of the demonstration setup. Further optimization is then performed on the three-stage dual-opposed FPSG system. This comprehensive approach, comprising theoretical analysis, numerical simulation, experimental assessment, and optimization aims to provide valuable insights into analyzing, designing, and enhancing multi-stage dual-opposed FPSG systems for efficient energy conversion and CHP applications.

2. System configuration and theoretical analysis

2.1 System configuration

The schematic diagram of the multi-stage FPSE-based cogeneration system proposed in this study is presented in Figure 1. This cogeneration system comprises multiple stages of dual-opposed FPSG, which are thermally coupled through a water circulation loop and a waste heat carrier delivery line. The waste heat carrier and circulating water flow sequentially through the HHX and ambient heat exchanger (AHX) of each stage. Each stage consists of two identical single FPSGs with a shared expansion space, effectively canceling vibrations between them. A single FPSG includes an acoustically coupled β -type FPSE and a moving-magnet-type linear alternator [38]. The FPSE primarily consists of an AHX, regenerator, HHX, and displacer resonating with planar springs. The linear alternator comprises a power piston supported by a gas bearing and an electromagnetic conversion circuit.

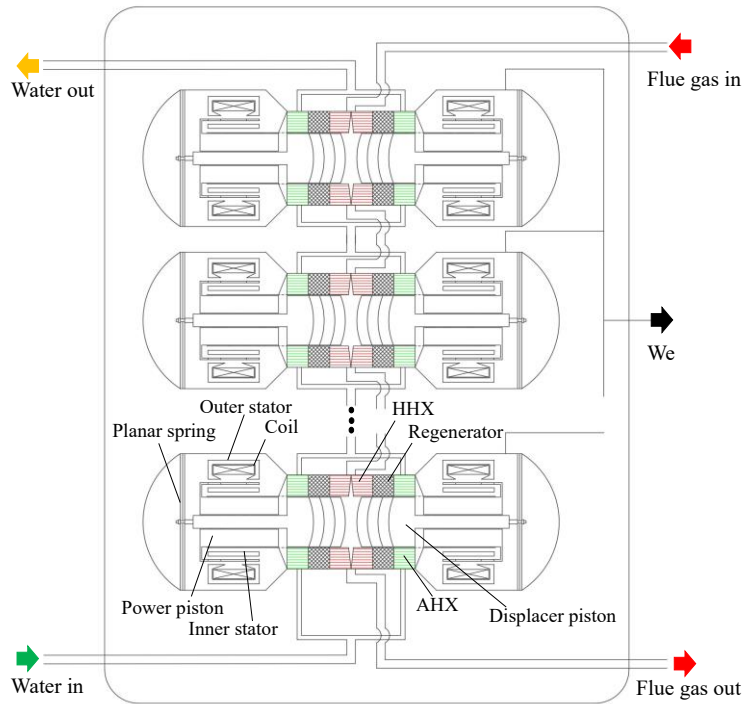


Figure 1 Schematic diagram of the multi-stage FPSE-based cogeneration system.

2.2 Theoretical analysis

Before proceeding with the simulation of the multi-stage FPSE-based cogeneration system, it is essential to establish a simplified thermodynamic equivalent model in order to enhance the understanding of exergy improvement through the adoption of multiple stages. As illustrated in Fig. 2, each FPSG within the multi-stage combined heat and power system operates as an ideal thermal-electric conversion unit that absorbs heat from a constant high-temperature source and converts it into electricity, while simultaneously dissipating waste heat to a constant low-temperature sink. This model facilitates a comprehensible analysis of exergy losses during the heat transport process. Taking flue gas as an example of a waste heat carrier, high-temperature flue gas enters the inlet of the first stage HHX, sequentially passes through each stage's HHX, and exits at the outlet of the final stage HHX (the lower-temperature flue gas discharged at this outlet can also be utilized in alternative ways). Throughout this process, the flue gas releases heat resulting in temperature reduction. It is assumed that the specific heat capacity of the flue gas remains independent of temperature, and there exists a uniform temperature difference between each stage's HHX inlet and outlet. The power conversion unit harnesses higher-temperature heat for electricity generation while utilizing lower-grade dumped heat for domestic hot water supply and space heating purposes.

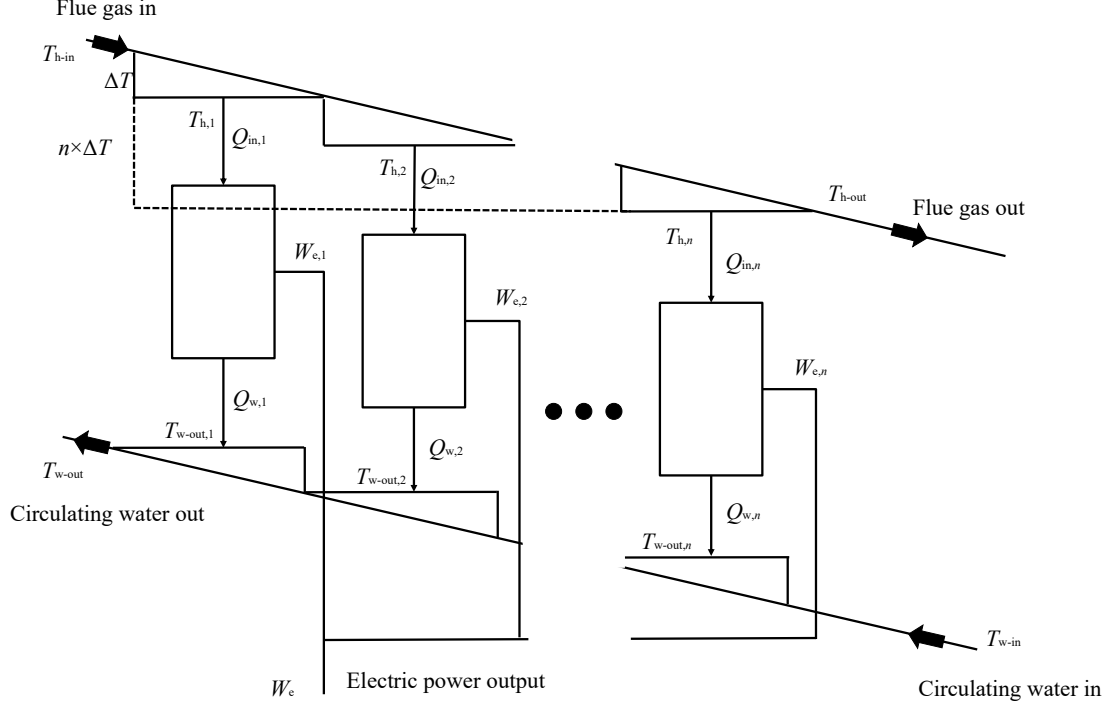


Figure 2 Thermodynamic equivalent model for the multi-stage combined heat and power system.

The total exergy E_{total} contained in the flue gas at the inlet of the first stage HHX could be written as

$$E_{\text{total}} = - \int_{T_{h-\text{in}}}^{T_0} \dot{m} c_p \frac{T - T_0}{T} dT = \dot{m} c_p (T_{h-\text{in}} - T_0) + \dot{m} c_p T_0 \ln \frac{T_0}{T_{h-\text{in}}} \quad (1)$$

Where \dot{m} and c_p are the mass flow rate and specific heat capacity of the flue gas, respectively. T_0 and $T_{h-\text{in}}$ denote the ambient temperature and the flue gas temperature at the inlet of the first stage HHX, respectively.

The maximal exergy E_{max} contained in the heat absorbed by all the HHXs in the cogeneration system could be written as

$$\begin{aligned} E_{\text{max}} &= - \int_{T_{h-\text{in}}}^{T_{h-\text{out}}} \dot{m} c_p \frac{T - T_0}{T} dT \\ &= \dot{m} c_p (T_{h-\text{in}} - T_{h-\text{out}}) + \dot{m} c_p T_0 \ln \frac{T_{h-\text{out}}}{T_{h-\text{in}}} \end{aligned} \quad (2)$$

Where $T_{h-\text{out}}$ denotes the flue gas temperature at the outlet of the last stage HHX.

Since the temperature difference between the inlet and outlet of each stage's HHX is assumed constant, hence the flue gas temperature at the i th stage's HHX outlet, T_i , can be formulated as

$$T_i = T_{h-\text{in}} - \frac{T_{h-\text{in}} - T_{h-\text{out}}}{n} i \quad (3)$$

where n is the total stage number of the cogeneration system. Accordingly, the actual exergy

utilized by the i th stage, E_i , and the total actual utilized exergy E_{actual} are calculated by using Eq. (4) and Eq. (5), respectively.

$$E_i = \dot{m}c_p \frac{T_{h\text{-in}} - T_{h\text{-out}}}{n} \frac{T_i - T_0}{T_i} \quad (4)$$

$$E_{\text{actual}} = \sum_{i=1}^n E_i \quad (5)$$

To assess the exergy utilization efficiency of the cogeneration system, three performance indexes are defined: the relative exergy utilization efficiency η_{rel} , the total exergy utilization efficiency η_{total} and the maximal exergy utilization efficiency η_{max} . The relative exergy utilization efficiency η_{rel} is the ratio of actual utilization exergy by the cogeneration system and the maximal exergy that can be utilized by the cogeneration system. The maximal exergy utilization efficiency η_{max} is the ratio of maximal exergy that can be utilized by the cogeneration system and the total exergy contained in the flue gas at the inlet of the first stage HHX. The total exergy utilization efficiency η_{total} is the ratio of the actual utilization exergy and the total exergy contained in the flue gas at the inlet of the first stage HHX, which can also be calculated as the product of η_{max} and η_{rel} .

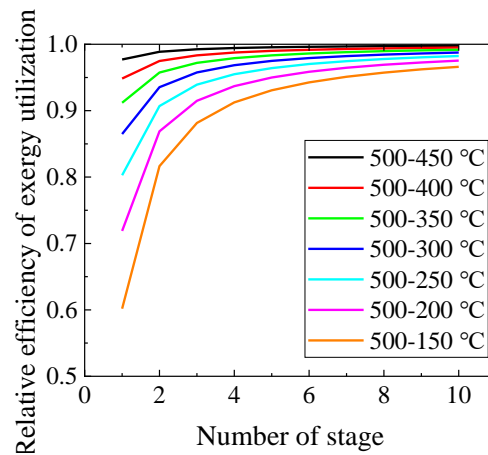
$$\eta_{\text{rel}} = \frac{E_{\text{actual}}}{E_{\text{max}}} \quad (6)$$

$$\eta_{\text{max}} = \frac{E_{\text{max}}}{E_{\text{total}}} \quad (7)$$

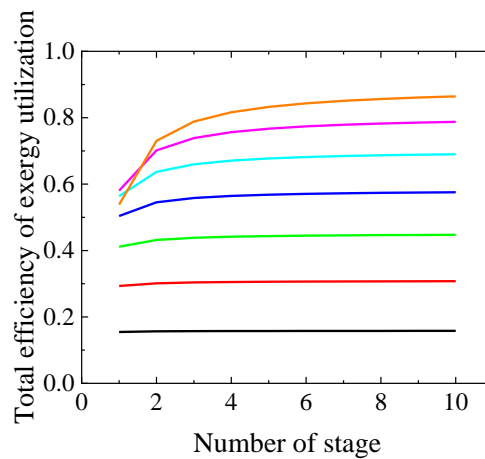
$$\eta_{\text{total}} = \frac{E_{\text{actual}}}{E_{\text{total}}} = \eta_{\text{max}}\eta_{\text{rel}} \quad (8)$$

Figure 3 gives the dependence of the exergy utilization efficiencies on the stage number, at different flue gas temperature differences between the inlet and outlet. As can be seen in Figure 3 (a), for a given flue gas temperature difference, the relative exergy utilization efficiency rises with the increase of stage number, especially evident at large flue gas temperature differences. For example, for a flue gas inlet temperature of 500 °C and an outlet temperature of 150 °C, the relative exergy utilization efficiency grows sharply with the increase of stage number when the stage number is below 4. However, when the stage number is above 4, the growth rate of the relative exergy utilization efficiency declines gradually. Figure 3 (b) further presents the total exergy utilization efficiency against the stage number. For large flue gas temperature differences between inlet and outlet, an increase in the stage number leads to a significant increase in the total exergy utilization efficiency when the stage number is below 4, whereas the slope edges down as the stage number increases. This implies that a multiple-stage system outperforms a single-stage system for the recovery of all or majority of the waste heat from the flue gas with a high total exergy utilization efficiency. However, the advantage of a multiple-stage system over a single-stage system would be undermined if a small temperature difference between the inlet and outlet is favored. In contrast to the relative exergy utilization efficiency, for a fixed stage number and a constant flue gas inlet temperature of 500 °C, the larger the flue gas temperature difference between the inlet and outlet, the larger

the total exergy utilization efficiency. Therefore, a three-stage cogeneration system for waste heat recovery is chosen and assessed in this work.



(a)



(b)

Figure 3 (a) The relative exergy utilization efficiency and (b) the total exergy utilization efficiency as functions of stage number, at different flue gas temperature differences between inlet and outlet (The legend of Figure 3 (b) is the same as that of Figure 3 (a)).

3. Modeling approach and validation

3.1 Modeling Approach

The three-stage FPSE-based cogeneration system was modeled with Gedeon Associate's Sage [39], a one-dimensional software package for modeling Stirling engines and coolers. The numerical model developed in Sage incorporates model instances for the heat exchangers, working space, regenerator, moving parts, and pressure source. These model instances are logically connected through mass flow, pressure wave, force, and energy flow to form an integrated model. Sage combines the motion equations of the piston and displacer with the Navier-Stokes equations and energy equations. Detailed one-dimensional governing equations for momentum, continuity, and energy in the gas domain for Sage can be found in Ref. [39]. It is worth noting that Sage is widely used as a thermodynamic modeling tool for Stirling engines

and coolers [34,40], thermoacoustic engines and coolers [41,42], as well as other regenerative heat engines [43], with its accuracy thoroughly validated through experiments.

In a previous study conducted by the authors' group [44], the HHX heat losses (including conduction and radiation) through the thermal insulation layer were tested on a single FPSG. Based on the test results, a function was derived to calculate the gross heating power of the single FPSG as a function of HHX wall temperature, which is incorporated in Eq. (9).

$$Q_{in} = Q_{in-num} + (0.0006T_h^2 + 2.2146T_h - 690.28) \quad (9)$$

where Q_{in} and Q_{in-num} are the gross heating power of the FPSG and the actual heating power entering the engine, respectively. T_h is the HHX wall temperature, and the polynomial in the parentheses denotes the heat dissipation at the HHX.

The gross rejected heat of each single FPSG mainly originates from three parts, the heat rejected at the AHX, the heat produced by the mechanical resistance, and the coil resistance. The gross rejected heat can be formulated as

$$Q_w = Q_c + Q_{damp} + Q_{coil} \quad (10)$$

where Q_w , Q_c are the gross rejected heat of each single FPSG and the heat rejected at the AHX, respectively. Q_{damp} and Q_{coil} are the heat produced by the mechanical resistance and the coil resistance, respectively, and they can be estimated by using Eq. (11) and Eq. (12).

$$Q_{damp} = \frac{1}{2}R_m|\hat{v}|^2 = \frac{1}{2}R_m(\omega\hat{X}_{amp})^2 \quad (11)$$

$$Q_{coil} = \frac{1}{2}R_{in}|\hat{I}|^2 \quad (12)$$

where R_m and v are the mechanical damping coefficient and velocity of a moving part, respectively, ω is the angular frequency, and X_{amp} is the displacement amplitude of a moving part. R_{in} and I are the internal resistance and current of the linear alternator, respectively. Since the gross rejected heat (also supply heat to circulating water) is finally taken away by the circulating water, so the gross rejected heat can also be written as:

$$Q_w = \dot{m}c_p(T_{w-out} - T_{w-in}) \quad (13)$$

where T_{w-out} and T_{w-in} are the inlet and outlet water temperatures, respectively.

For the linear alternator, its governing equations in the frequency domain is given as follows.

Force balance equation:

$$\hat{p}_{comp}A_p = \tau\hat{I} + (R_{mp} + i\omega M - i\frac{K_p}{\omega})\hat{v} \quad (14)$$

Electrical balance equation:

$$\tau\hat{v} = (R_{in} + R_{out} + i\omega L - i\frac{1}{\omega C})\hat{I} \quad (15)$$

where p_{comp} represent the pressure wave amplitude in the compression space. A_p and τ are the cross-sectional area of the power piston and the force factor of the linear alternator,

respectively. i is the imaginary unit, and ω is the angular frequency. R_{mp} and M denote the mechanical damping coefficient and moving mass of the power piston, respectively. K_p represents the spring stiffness of the power piston. R_{in} , R_{out} , L and C are internal resistance, external load resistance, electric inductance, and electric capacitance respectively of the linear alternator.

Acoustic impedance is a key parameter to evaluate the coupling between an acoustic source and acoustic load in thermoacoustic systems, it denotes the ratio between local complex pressure and local complex volume flow rate, i.e.,

$$\hat{Z} = \frac{\hat{p}}{\hat{U}} = \text{Re}(\hat{Z}) + i \cdot \text{Im}(\hat{Z}) \quad (16)$$

The linear alternator acts as an acoustic load to the FPSE, and its acoustic impedance can be derived theoretically by combining Eq. (14) and Eq. (15):

$$\hat{Z}_{LA} = \frac{1}{A_p^2} \left[\left(R_{mp} + \frac{\tau^2}{R_{in} + R_{out}} \right) + i \left(M\omega - \frac{K_p}{\omega} \right) \right] \quad (17)$$

From the viewpoint of thermoacoustics, an FPSG is an acoustic resonance system that works by matching the acoustic impedances of the FPSE and linear alternator under the same conditions [45]. Therefore, this unique principle could be quantified as

$$\hat{Z}_{engine} = \hat{Z}_{LA} \quad (18)$$

where \hat{Z}_{engine} represents the acoustic impedance at the surface of the power piston facing FPSE, i.e., the acoustic impedance provided by the FPSE. Eq. (18) forms a constraint for the motion of the power piston, to couple the FPSE and the linear alternator in the developed model. By integrating these equations, a thermal-dynamic-electric fully-coupled numerical model for a single FPSG was established accordingly.

Based on the developed single FPSG numerical model, the three-stage FPSE-based cogeneration system was modeled by thermally coupling the two adjacent stages of dual-opposed FPSG. The flow chart of the numerical simulation for the three-stage system is presented in Figure 4. On the premise of the initial flue gas inlet temperature, supply water temperature (i.e., the water outlet temperature of the system), and the flow rate of the circulating water, the state parameters of the first stage (i.e., the temperature of the HHX and the outlet water of AHX, and gross input heating power) are obtained, then the rejected heat at the AHX of the first stage dual-opposed FPSG is calculated. According to the obtained rejected heat, the inlet water temperature (also the outlet water temperature of the adjacent stage) and temperature lift through the AHX of the first stage are derived. The second and third stages follow the same procedure.

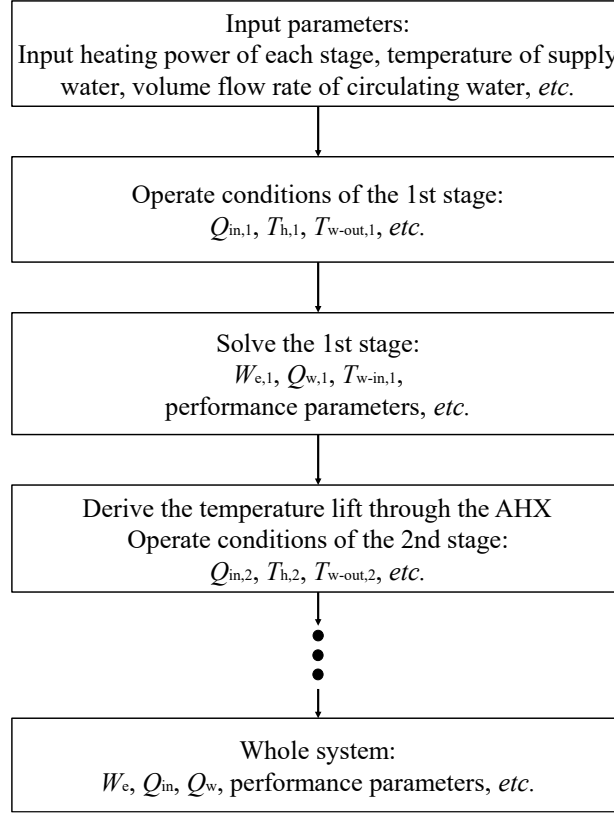


Figure 4 Flow chart of the numerical simulation for the three-stage system.

To evaluate the CHP performance of the single-stage dual-opposed FPSG as well as the three-stage dual-opposed FPSG, some performance indexes are defined herein. The acoustic power output by the FPSE is expressed as:

$$W_a = \frac{1}{2} |\hat{p}_{comp}| |\hat{U}_p| \cos \theta_{pU} \quad (19)$$

where \hat{p}_{comp} represents the complex pressure wave in the compression space and \hat{U}_p is the complex volume flow rate at the interface of the power piston. θ_{pU} is the phase difference between the pressure wave and the volume flow rate. The acoustic-to-electric efficiency (i.e., the linear alternator efficiency) of a single-stage dual-opposed FPSG is defined as:

$$\eta_{LA} = \frac{W_e}{W_a} \quad (20)$$

In addition, the thermal-to-electric efficiency η_{t-e} and the overall efficiency (i.e., the CHP efficiency) η_{CHP} of a single-stage dual-opposed FPSG are calculated by the following formulas, respectively.

$$\eta_{t-e} = \frac{W_e}{Q_{in}} \quad (21)$$

$$\eta_{CHP} = \frac{W_e + Q_w}{Q_{in}} \quad (22)$$

Similarly, the thermal to electric efficiency η_{t-e} and the overall efficiency (i.e., the CHP efficiency) η_{CHP} of the three-stage dual-opposed FPSG can be estimated by using Eq. (23) and Eq. (24).

$$\eta_{t-e} = \frac{\sum_{i=1}^3 W_{e,i}}{\sum_{i=1}^3 Q_{in,i}} \quad (23)$$

$$\eta_{\text{CHP}} = \frac{\sum_{i=1}^3 (W_{e,i} + Q_{w,i})}{\sum_{i=1}^3 Q_{in,i}} \quad (24)$$

where $W_{e,i}$, $Q_{w,i}$, and $Q_{in,i}$ represent the output electric power, gross rejected heat and gross input heating power of the i th stage dual-opposed FPSG, respectively.

3.2 Model validation

The accuracy of the developed numerical model was validated by using a laboratory-built single-stage dual-opposed FPSG prototype (which consists of two identical single-piston FPSG units). A series of experiments were conducted under different mean pressures and heating temperatures. Figure 5 illustrates the schematic diagram of the dual-opposed FPSG, while Figure 6 presents a photograph of the actual prototype. Table 1 provides detailed dimensions of each single-piston FPSG unit. The test system employed for evaluating the dual-opposed FPSG prototype is similar to that used for the three-stage dual-opposed FPSG, with further details provided in Section 5.1.

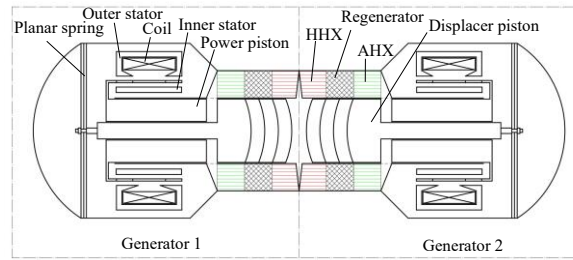


Figure 5 Schematic of the single-stage dual-opposed FPSG.

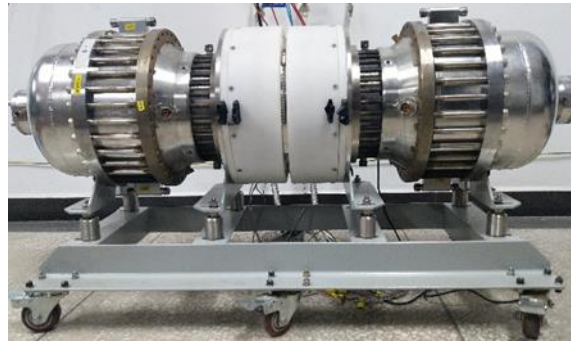


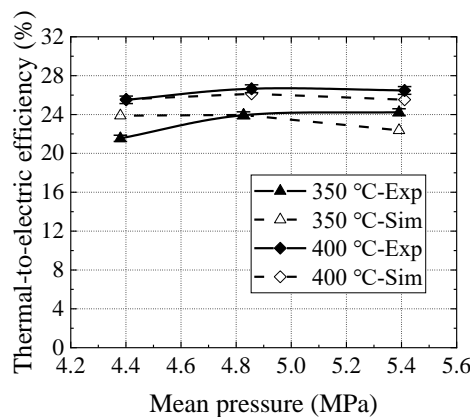
Figure 6 Photograph of the single-stage dual-opposed FPSG.

Table 1 Detailed dimensions of the updated FPSG

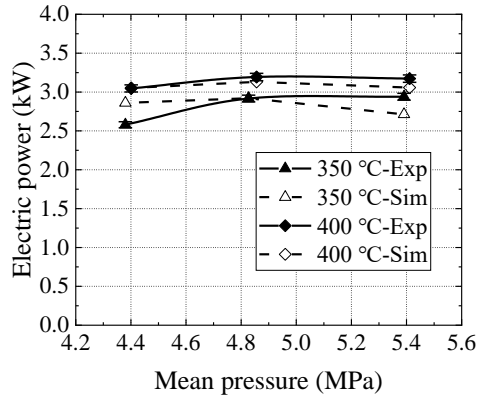
Part	Component	Detailed Dimensions
FPSE	AHX	Shell-and-tube type, length 65 mm, shell ID 0.12 m, OD 0.22 m, tube ID 2.5 mm, number 432
	Regenerator (REG)	Length 60 mm, equivalent diameter 145 mm, filled with stainless steel random fiber, wire diameter 16

		μm, porosity of 90%
	Displacer (DISP)	Diameter 120 mm facing expansion space, diameter 116 mm facing compression space, equivalent moving mass 3.7 kg, spring constant 380 kN/m, nominal mechanical resistance around 30 N/s
	HHX	Radial-fin type, length 67 mm, width 1 mm, height 9.4 mm, number of fins 360
	Power piston (PIST)	Equivalent diameter 116 mm, moving mass 6 kg
Linear alternator	Alternator	Force factor 105 N/A (FEA nominal value), magnetic spring stiffness 150 kN/m, coil resistance 0.3 Ω

The obtained experimental results are then compared with the numerical results on the single-stage system, as depicted in Figure 7. Figure 7 (a) illustrates the thermal-to-electric efficiency calculations and experiments for different HHX wall temperatures against mean pressure. The gross heating power was consistently set at 12 kW in both simulations and experiments. The volume flow rate and inlet temperature of cooling water were maintained at 2 m³/h and 20 °C, respectively. Figure 7 (b) presents the output electric power calculations and experiments for various HHX wall temperatures across mean pressure values. As observed in Figure 7, the maximum deviation between calculated and experimental results is within a range of 10%. Figure 8 showcases the displacement amplitude of the power piston calculations and experiments for different HHX wall temperatures against mean pressure. It is evident that the calculated piston displacement amplitudes align well with experimental observations. Additionally, an intriguing finding emerges: for a same charge pressure, when the heating temperature decreases from 400 °C to 350 °C, there is a roughly one-millimeter increase in displacement amplitude of the power piston, which serves as a primary factor contributing to lower efficiency. Undoubtedly, these current agreements between experiments and calculations effectively demonstrate the validity of our modeling approach.



(a)



(b)

Figure 7 (a) Experiment and simulation results of thermal to electric efficiency versus mean pressure for different HHX wall temperatures, and (b) electric power versus mean pressure for different HHX wall temperatures.

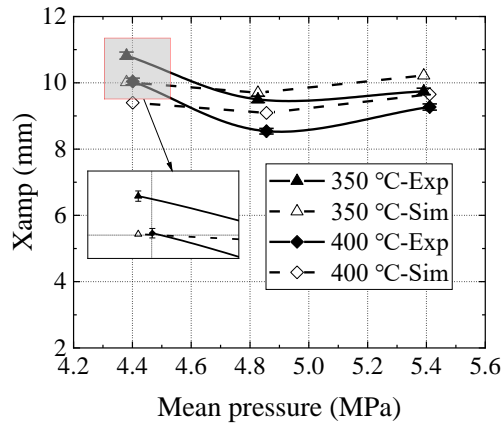


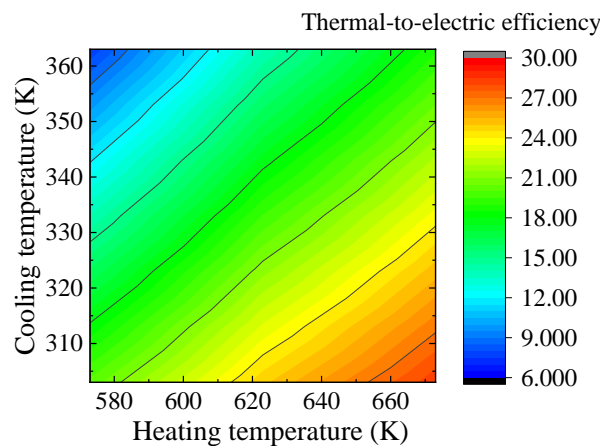
Figure 8 Experiment and simulation results of displacement amplitude of power piston versus mean pressure for different heating temperatures.

4. Numerical results and discussions

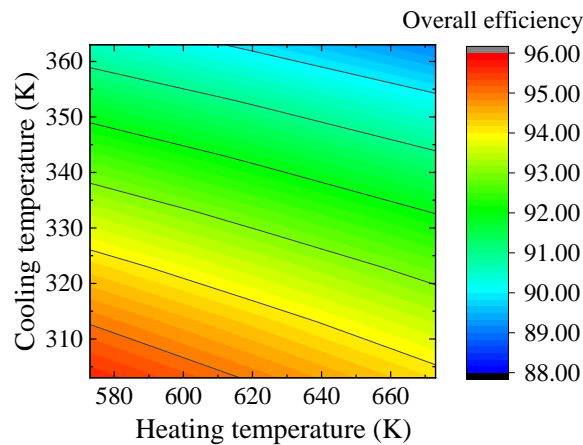
Based on the validated numerical model, the performance of a three-stage FPSE-based cogeneration system was further studied numerically. The schematic of the studied system follows the fundamental layout presented in Figure 1 but with three stages. The system consists of three identical thermally-coupled dual-opposed FPSGs, as studied in the previous section. In simulations, according to the above assumptions, the HHX heating temperature of the first, second, and third stages are 400 °C, 350 °C, and 300 °C, respectively, and the heating power at each stage is 20 kW. The water inlet temperature of the system is presumed to be nearly constant (environment temperature). In order to satisfy the household space heating and domestic hot water demands, a series of cold end temperatures ranging from 30 °C to 90 °C is studied.

It's been pointed out that the dimensions of each FPSG are identical but with slight differences in their operating temperatures (i.e., heating temperature and the cold end

temperature), thereby to simplify the calculation, a single FPSG's performance was studied at different temperature conditions when the mean pressure and input heating power are 5 MPa and 20 kW respectively. Figure 9 (a) is the contour of the thermal to electric efficiency. Figure 9 (b) illustrates the contour of the overall efficiency. As shown in Figure 9 (a), the thermal-to-electric efficiency drops with decreasing temperature ratio, which is roughly proportional to the descent in Carnot efficiency. With the temperature ratio decreasing from 2.22 to 1.58, the thermal-to-electric efficiency declines from 28.38% to 7.60%. The difference in the trend of the thermal to electric efficiency and the overall efficiency could be attributed to the energy loss caused by heat radiation or natural convection to the environment. It should be noted that heat loss increases with the rise of mean temperature; thus, the CHP efficiency decreases from 95.64% to 89.09%.



(a)

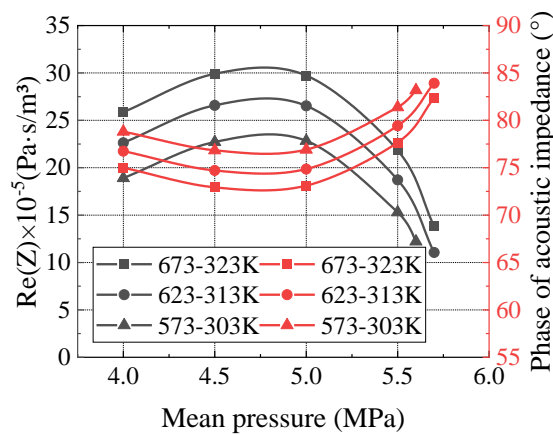


(b)

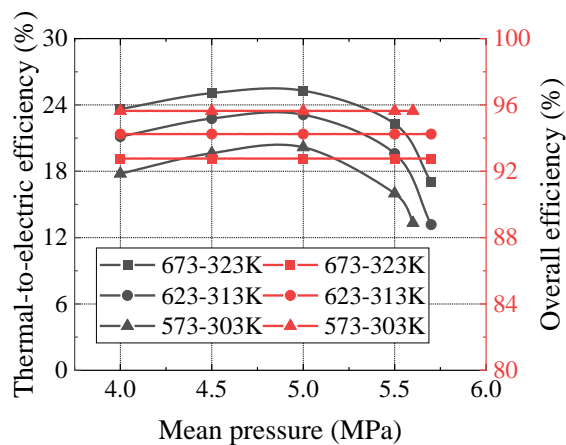
Figure 9 (a) Influence of the heating temperature and the cold end temperature on thermal to electric efficiency, and (b) influence of the heating temperature and the cold end temperature on overall thermal efficiency.

The effect of the mean pressure on the system performance was subsequently explored. Figure 10 (a) shows the influence of mean pressure on the real part and phase angle of the acoustic impedance provided by the FPSE, and Figure 10 (b) shows the FPSG's performance

variation curves with different mean pressures. Both figures stand for a single FPSG at different temperature conditions. The FPSG's performance curves show that there is an optimal mean pressure close to 4.8 MPa beyond which the thermal-to-electric efficiency would otherwise deteriorate. The variation curve of acoustic impedance at the coupling interface reveals the underlying mechanism. According to the deduced expression (Eq. (17)) of acoustic impedance from the viewpoint of a linear alternator with the variation of mean pressure, the external electric resistance changes to meet the requirement of acoustic resonance. The real part of the acoustic impedance is a representation of acoustic power output, and the phase angle of the acoustic impedance is a representation of thermoacoustic conversion efficiency. Generally, the larger the real part of the acoustic impedance, the more the thermal power is converted into acoustic power, and the closer the phase angle approaches 90° , the lower the thermoacoustic conversion efficiency. As a matter of fact, when the mean pressure changes, the operating frequency varies correspondingly, which in turn alters the phase-shifting effect of the displacer. Fundamentally, when the operating frequency is close to the stand-alone resonant frequency of the displacer, the thermal-to-electric efficiency would be better. On the contrary, for a fixed heating temperature and cold end temperature, the CHP efficiency is almost independent of the mean pressure, as is known that the thermal loss is just affected by the temperature of the system.



(a)



(b)

Figure 10 (a) Effect of mean pressure on the acoustic impedance, and (b) single-stage FPSG CHP performance versus the mean pressure.

By implementing the uncoupling method shown in Figure 4, the three-stage FPSE-based cogeneration system was modeled. The design point with 20 kW input heating power in each stage has been simulated and analyzed.

Figure 11 is a comparison of exergy loss in each stage. The heating temperatures for the 1st, 2nd, and 3rd stage are 400 °C, 350 °C and 300 °C, respectively. With the increase of stage numbering, AEFric, AEQw, and AEdamp all increase obviously. The difference between the 1st stage's total exergy loss and that of the 3rd stage is close to 400 W, the difference in the phase of the two stages' acoustic impedances (as shown in Figure 10 (a), a lower temperature ratio corresponds to a higher phase of acoustic impedance) is the main reason for the total exergy loss difference. The considerable exergy loss in the 3rd stage implies that there is a higher exergy loss in the lower heating temperature stage.

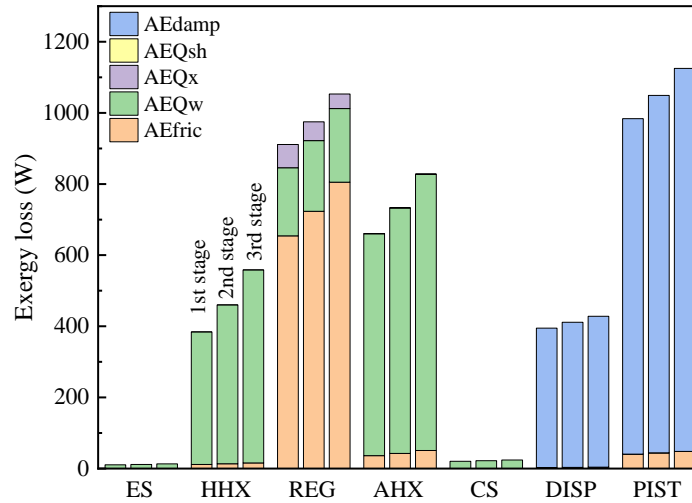


Figure 11 Exergy loss comparison of different stages in the three-stage FPSG prototype: AEdamp, available energy loss caused by mechanical damping; AEQsh, AE loss caused by shuttle; AEQx, AE loss caused by x-direction conduction; AEQw, AE loss caused by wall-to-gas heat exchange; AEFric, AE loss caused by flow friction.

Combined with the exergy analysis in Section 2.2, Fig. 12 shows a comparison of a single-stage system and a three-stage system on different components' exergy proportions. The exergy loss caused by the temperature difference between the heat carrier and wall of HHX (shortened as DT in Fig. 12) decreases from 11.4% (single-stage system) to 3.7% (three-stage system). Except for the heat loss from the shell (shortened as Shell in Fig. 12) to the environment, the other components of the three-stage system have lower exergy loss in comparison with that of the single-stage system. The exergy efficiency calculated through electric power increases from 36.3% (single-stage system) to 43.9% (three-stage system), with a corresponding relative improvement of more than 20%.

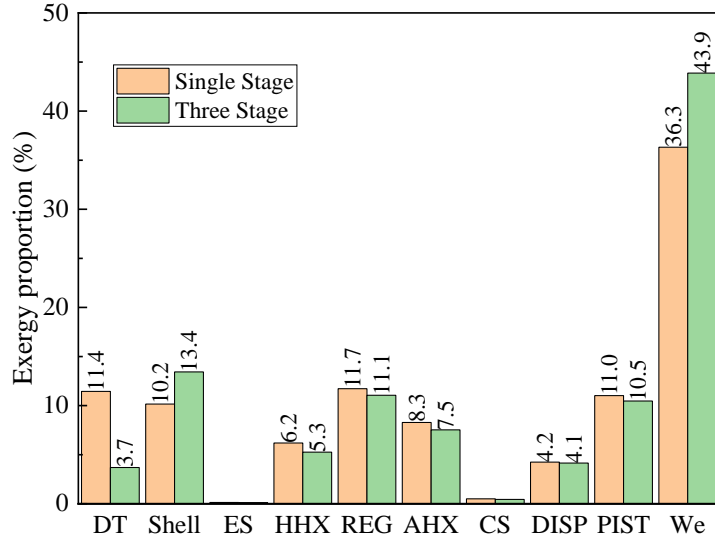


Figure 12 Comparison of single-stage system and three-stage system on different components' exergy proportion.

Figure 13 illustrates the thermal to electric efficiency and the overall efficiency of the three-stage system at different input heating powers. The mean pressure of the system is 5 MPa, the supply water temperature is 50 °C, and the circulating water volume flow rate is 2 m³/h. With the increase of input heating power (note that the abscissa of Figure 13 is the input heating power of the individual stage), the thermal to electric efficiency ascends slightly, and there is a close 1% improvement, which could be attributed to the drop of the proportion of thermal loss to the input heating power. Likewise, the variation trend of CHP efficiency of the three-stage system shows a slight uptick, close to 4%.

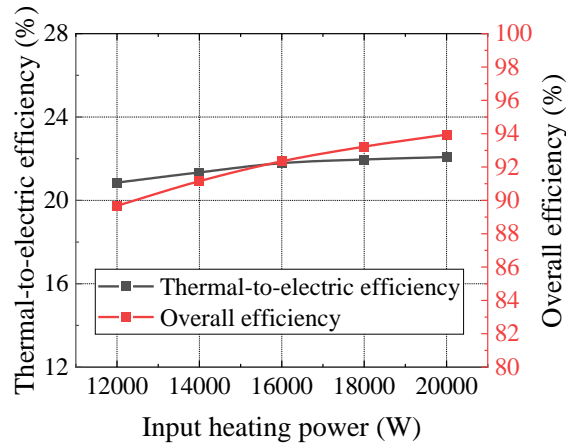
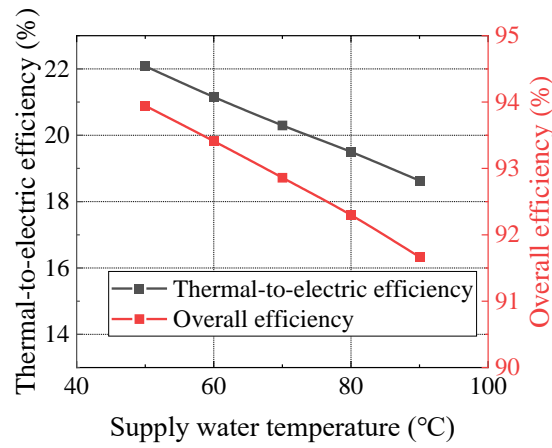


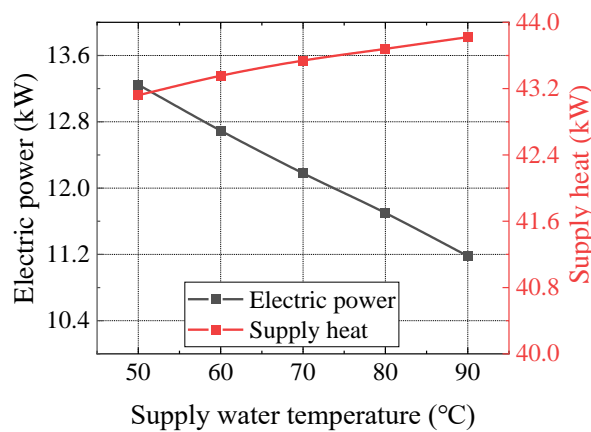
Figure 13 Three-stage system performance versus the input heating power.

Figure 14 shows the dependence of the three-stage FPSE-based cogeneration system's performance on the supply water temperature when the input heating power of each stage is 20 kW and the mean pressure is 5 MPa. As shown in Figure 14 (a), the thermal-to-electric efficiency decreases from 21% to 16% with the increase in supply water temperature because it is related to the reduction in the temperature ratios. Meanwhile, due to the rise of the AHX temperature, the overall efficiency of the whole system decreased from 94.5% to 91.6%. As

presented in Figure 14 (b), the output of electric power declines with the growth of the supply water temperature, from 50 to 90 °C, output of electric power decreases from 13.2 to 11.2 kW, while the thermal production of the cogeneration system increases with the growth of the supply water temperature since more heat is rejected under a lower temperature ratio.



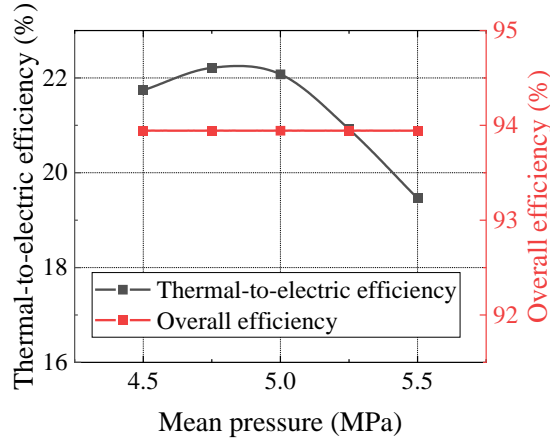
(a)



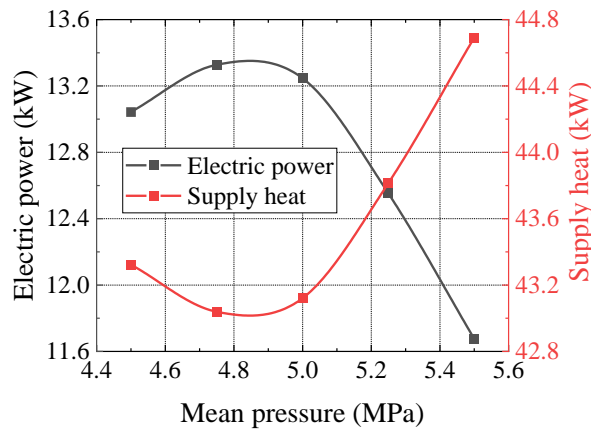
(b)

Figure 14 (a) The efficiency and (b) the electric power and supply heat of three-stage system performance versus supply water temperature.

Figure 15 (a) gives an explicit picture of how the mean pressure affects the thermal to electric efficiency and the system CHP efficiency when the input heating power of each stage is 20 kW, and the supply water temperature is 50 °C. Maximum thermal-to-electric efficiency higher than 22% is reached, which is consistent with the thermal-to-electric efficiency curve of the single FPSG as indicated in Figure 10. Meanwhile, the CHP efficiency of the three-stage system almost keeps constant with the increase of mean pressure. Figure 15 (b) further gives the dependence of electric power and supply heat on the mean pressure. It can be seen that with the growth of mean pressure, the variation trend of output electric power is the same as that of the thermal to electric efficiency (since the gross input heating power of the cogeneration system remains constant), but the variation trend of supply heat is roughly opposite, resulting in an almost constant cogeneration power (output electric power plus supply heat).



(a)



(b)

Figure 15 (a)The efficiency and (b) the electric power and supply heat of the three-stage system versus the mean pressure.

5. Experiments and discussions

The three-stage FPSE-based cogeneration demonstration setup was constructed using explicit simulations, and subsequent experiments were conducted to assess the system's performance. This section provides a comprehensive account of the experimental setup, results, discussions, and suggestions for further enhancement.

5.1 Experiment setup

The objective of the experiments is to comprehend the operational characteristics of the three-stage FPSE-based cogeneration system and validate the feasibility of such a cascade layout. To ensure precise measurement accuracy for input heating power, thereby guaranteeing accurate assessment of thermal-to-electric conversion performance, electric heaters are utilized in experiments to simulate variable-temperature heat sources. The use of electric heaters also eliminates complexities associated with flue gas heating systems in terms of layout and control, while providing greater convenience in adjusting heating power and temperature compared to flue gas heating systems. Figure 16 presents the schematic diagram of the three-stage FPSE-

based cogeneration demonstration setup, comprising three independent electrical heating sub-systems, three dual-opposed FPSGs, a water-circulating sub-system, three electrical load sub-systems, and a data acquisition sub-system. Figure 17 depicts a photograph showcasing the three-stage FPSG system.

For the electrical heating sub-systems, the input heating power of each dual-opposed FPSG is supplied by electric cartridge heaters (embedded in the heater head of the FPSG) and measured using corresponding power meters (model AN8711P, with an indication error of $\pm 0.4\%$ plus a full-scale error of $\pm 0.4\%$). Multiple K-type thermocouples (with an accuracy of ± 1 K) are positioned at the heater head of each individual FPSG to measure the temperature on the heater head wall (designated as T1–T6). Additionally, a Collihigh pressure transmitter (with an accuracy class of 0.25) is installed in the bounce space of each dual-opposed FPSG to measure its mean pressure.

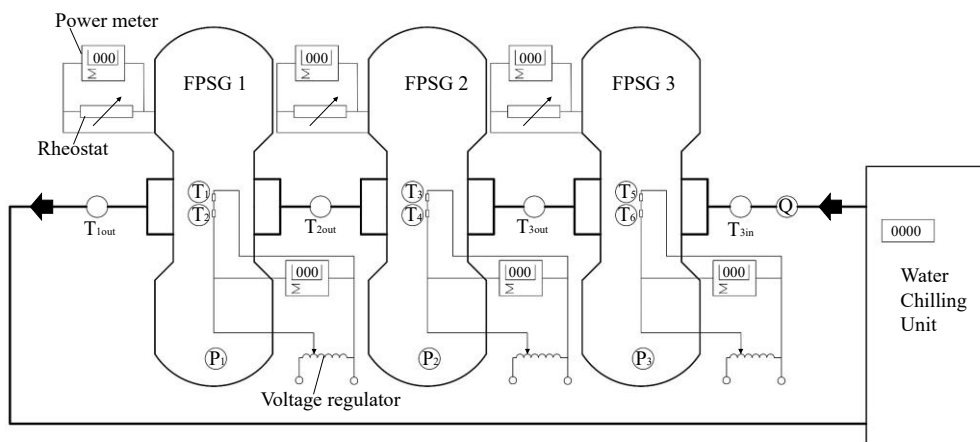


Figure 16 The schematic of the three-stage FPSE-based cogeneration demonstration setup.

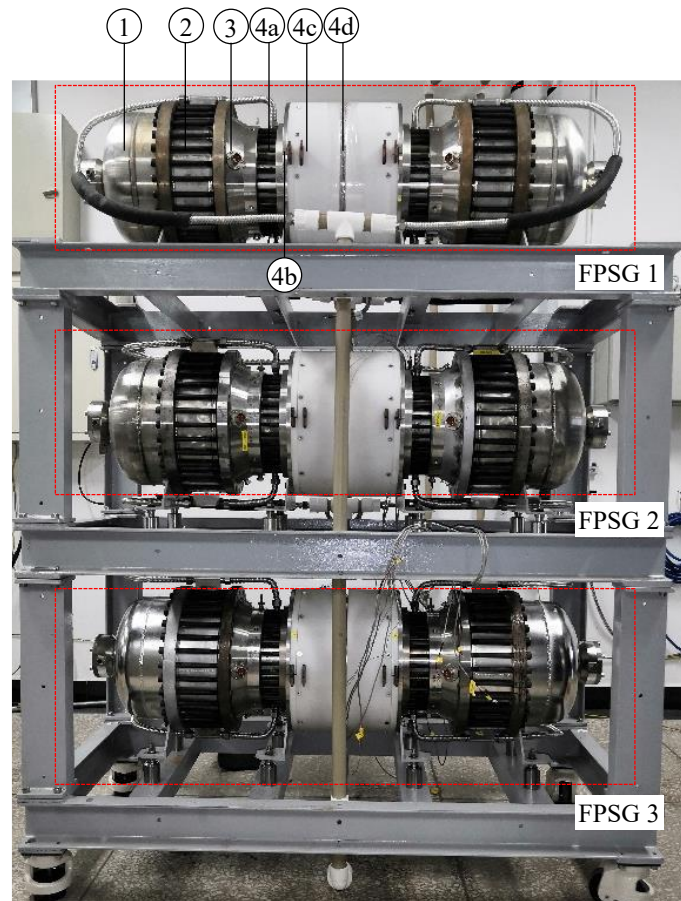


Figure 17 Photograph of the three-stage FPSG system: 1, bounce space; 2, linear alternator; 3, compression space; 4a, AHX; 4b, regenerator; 4c, heating block; 4d, expansion space.

In the water-circulating sub-system, an industrial water chiller was employed to absorb waste heat produced by the system. It should be noted that the temperature control precision of this chiller is quite limited and the refrigeration compressor will start and stop intermittently, thereby causing fluctuations in the cooling water temperature. The circulating water initially enters the AHX of the third stage dual-opposed FPSG from a water chilling unit to absorb the rejected heat. Subsequently, it sequentially passes through the AHXs of the second and first stages. Finally, the heated circulating water is returned to the water chilling unit for cooling and recycling purposes. Four platinum resistance thermometers (with an accuracy of ± 0.15 K) are installed at specific locations: inlet and outlet of the AHX in the third stage dual-opposed FPSG, outlet of AHX in the second stage, and outlet of AHX in the first stage respectively, to measure local water temperatures. Additionally, a turbine flowmeter (with an accuracy of $\pm 0.5\%$) is connected in series within the water circulation loop to determine the volume flow rate.

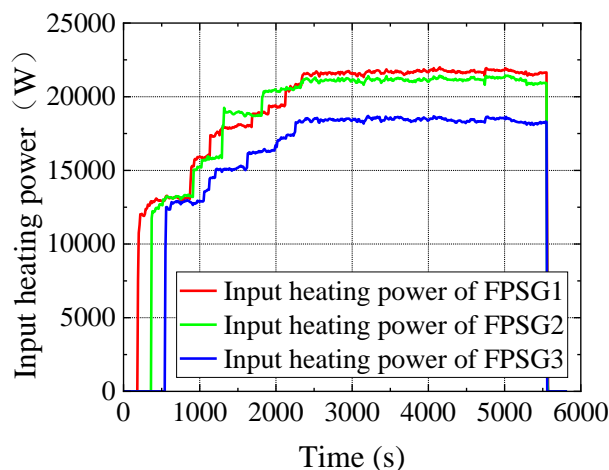
Regarding the electrical load sub-systems, each stage of the dual-opposed FPSG is connected to an independent load sub-system, enabling individual control over the heating temperature by adjusting the external load (i.e., rheostat). The power consumption of each load sub-system, which serves as a measure for characterizing the output electric power of each dual-opposed FPSG, is assessed using a current probe (TCPA300) with an accuracy of $\pm 1\%$, a differential voltage probe with an accuracy of $\pm 1\%$, and a NAPUI power meter (model PM9840)

with an error margin of $\pm 0.4\%$ indication error plus $\pm 0.1\%$ full scale. The displacement amplitude of the power piston is measured by a miniature piezoelectric uniaxial acceleration sensor (model 353B18, PCB Piezotronics, non-linearity $\leq 1.0\%$ in full scale). Finally, the error analysis method employed for these measurements aligns with that described in Ref. [34].

5.2 Experimental results and discussions

Experimental tests were conducted using the constructed demonstration setup to assess the performance of the system. Figure 18 illustrates the variations in input heating power, heating temperature, inlet water temperature at the AHX, and output electric power for each stage of the dual-opposed FPSG during a typical transient operation. As depicted in Figure 18 (a), in order to minimize mutual interference, heat input into each stage was not initiated simultaneously during experiments. The initiation processes resemble those of a single FPSG but with slight differences in threshold temperature. For the first stage dual-opposed FPSG, net electric power production commences when the wall temperatures of both HHXs reach $135.1\text{ }^{\circ}\text{C}$ and $136.0\text{ }^{\circ}\text{C}$ respectively. Once these wall temperatures rise to $120.3\text{ }^{\circ}\text{C}$ and $122.8\text{ }^{\circ}\text{C}$ for both HHXs, continuous oscillation is stimulated as part of the second stage's operation process. The onset HHX wall temperatures for the third stage are recorded as $135.7\text{ }^{\circ}\text{C}$ and $132.3\text{ }^{\circ}\text{C}$ respectively. It is important to note that the large-scale industrial water chilling unit used in the tests has limitations in temperature control precision. As depicted in Figure 18 (c), this leads to noticeable fluctuations in the water inlet temperature at the third stage AHX, consequently causing similar variations in other dynamic parameters during the experiments.

In experimental settings, the cogeneration demonstration setup is considered to operate under steady-state conditions when the inlet water temperature at each dual-opposed FPSG's AHX remains cyclically stable, allowing for fluctuations. It should be noted that despite careful handling, visible differences in heating power and desired heating temperature are inevitable due to complex thermal coupling and individual discrepancies. For an input heating power combination of 21.8 kW for the first stage, 21.3 kW for the second stage, and 18.6 kW for the third stage, corresponding heating temperatures of $418.7\text{ }^{\circ}\text{C}$, $348.2\text{ }^{\circ}\text{C}$, and $302.8\text{ }^{\circ}\text{C}$ are achieved respectively. Additionally, the water temperature at the outlet of the first stage AHX is measured as $50.2\text{ }^{\circ}\text{C}$ while it is recorded as $30.7\text{ }^{\circ}\text{C}$ at the inlet of the third stage cooler unit. Detailed performance data (with relative errors presented in brackets) of this cogeneration demonstration setup under steady-state conditions can be found in Table 2.



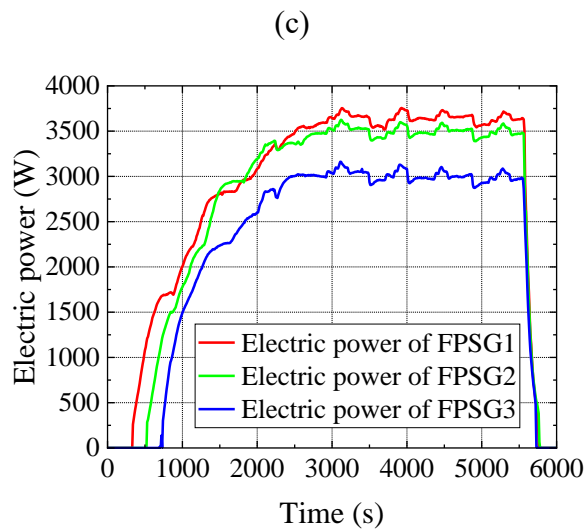
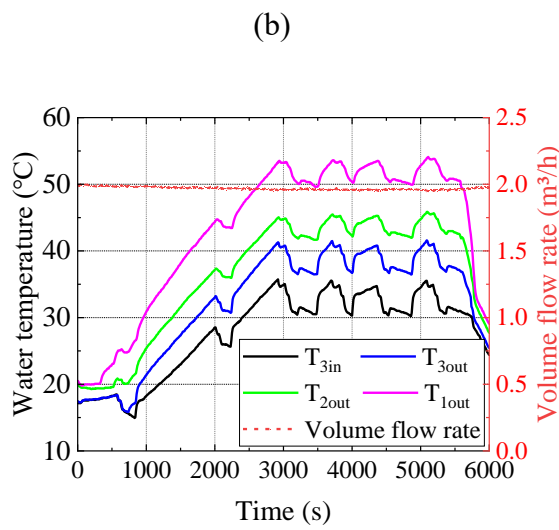
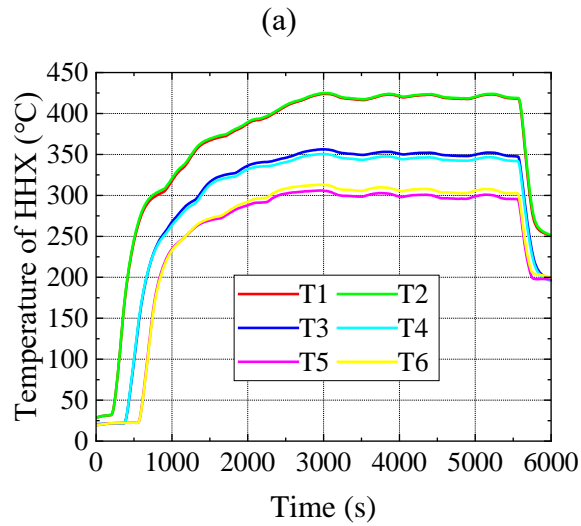


Figure 18 (a) Input heating power, (b) temperature of HHXs, (c) water temperature and volume flow rate, (d) output electric power versus time during a typical transient operation.

Table 2 Operating conditions and performance parameters of each stage and the whole

system under the steady-state condition

parameters	The 1st stage	The 2nd stage	The 3rd stage	Whole system
Mean pressure (MPa)	5.33	5.25	5.16	-
Heating temperature (K)	691.85	621.45	575.95	-
Input heating power (W)	21845.5	21292.9	18649.4	61787.8
Output electric power (W)	3667.3	3512.5	3004.7	10184.5
Rejected heat (W)	18197.6 (±4.3%)	12381.0 (±6.1%)	14145.8 (±5.4%)	44724.4 (±2.0%)
Outlet temperature of AHX (K)	323.37	315.43	310.03	303.85-323.37
Outlet and inlet water temperature difference at each stage (K)	7.94	5.40	6.18	19.52
Thermal to electric efficiency (%)	16.79 (±1.57%)	16.50 (±1.59%)	16.11 (±1.71%)	16.48 (±1.62%)
Overall efficiency (%)	100.09 (±4.5%)	74.64 (±5.7%)	91.96 (±5.5%)	88.87 (±2.7%)

According to the table, the overall thermal-to-electric efficiency of the three-stage thermally coupled free-piston Stirling cogeneration system is 16.48%, and the overall efficiency is 88.87%. It is noteworthy that the measured overall efficiency of the first-stage FPSG slightly exceeds 100% due to measurement error. To ensure a fair comparison, corresponding adjustments are made to the heating temperature settings (as shown in Table 2) in the numerical simulation to maintain consistency with experiments. The updated numerical result for thermal to electric efficiency yields 21.91%, and the overall efficiency reaches 94.06%. However, it should be noted that there exists a discrepancy between experimental and numerical results regarding both overall and thermal-to-electric efficiencies. Several factors contribute to this deviation. In our numerical model, losses caused by temperature drop during the heat exchange process, mechanical resistance, eddy current of a linear alternator, etc., are equivalently accounted for but may have been underestimated to some extent. Furthermore, differences in structural parameters between the prototype and numerical model could also account for this disparity (in our numerical model all structure parameters of each stage FPSG were assumed identical while maintaining such consistency among different FPSG prototypes can be challenging). Additionally, certain multidimensional effects such as temperature gradient resulting from circumferential heat transfer difference or pressure gradient arising

from nonuniform flow resistance were not incorporated into our numerical model.

Both the simulation and the experiment show the system's relatively low thermal-to-electric efficiency. This is mainly because the single-piston FPSG unit used to build the three-stage FPSE-based cogeneration demonstration setup was originally designed for a higher temperature ratio and a higher output electric power level [44] than those in this work. It has been pointed out that the temperature ratio imposes a significant impact on the optimum displacement of the piston and acoustic impedance, as shown in Figures 8 and 10. For a preliminary exploration of the potential, some key operational parameters and geometry parameters of the single FPSG module were optimized. Specifically, mean pressure, regenerator and void volume on the engine side, and effective cross-sectional area of the power piston on the linear alternator side, were opted for an attempt. As for the mean pressure, a higher one is favored to reduce the stroke of the power piston and in turn the frictional loss. While for the engine side, smaller dead volume and shorter regenerator, are preferred to achieve a higher dynamic pressure amplitude. Regarding the linear alternator, a larger diameter of the power piston leads to a larger sweep volume, which is also conducive to a lower frictional loss. In addition, a single temperature ratio, i.e., $T_h/T_c=573/343$ was assigned for simplicity.

Figure 19 illustrates the performance comparisons of the prototype model and optimized models. The thermal conditions of the three-stage system remain the same as that in Figure 11, i.e., the supply water temperature being 50 °C and the circulating water volume flow rate being 2 m³/h. It's obvious that thermal-to-electric efficiency exhibits notable improvement against the current prototype. Optimization on the engine outperforms the others in terms of performance improvement potential, implying the significance of acoustic field re-tuning regarding the temperature ratio variation. Optimization on the LA results in the smallest improvement in performance. With the increase of power piston diameter, loss pertaining to the clearance seal would increase accordingly, and this is the reason for the smallest performance improvement. Finally, the thermal-to-electric efficiency of the system is increased to above 25%, which is 20% higher than the benchmark. It is anticipated that the performance of the three-stage FPSE-based cogeneration demonstration setup can be further improved if a system-level optimization is conducted.

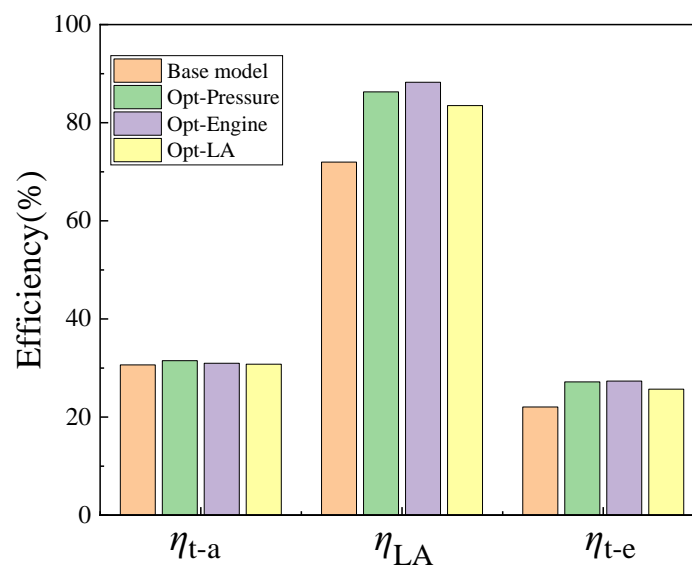


Figure 19 The performance comparisons of the baseline model and optimized models: η_{t-a} , thermal to acoustic efficiency; η_{LA} , acoustic to electric efficiency; η_{t-e} , thermal to electric efficiency.

6. Conclusions

To recover waste heat efficiently, this study proposes a thermally-coupled multi-stage free-piston Stirling engine-based cogeneration system that is capable of utilizing variable-temperature heat sources. To demonstrate the feasibility of such a system, a three-stage free-piston Stirling engine-based cogeneration system is numerically studied firstly based on a numerical model that has been validated on a single-stage system. Then, a demonstration setup was constructed and tested under both transient and steady-state conditions. Finally, the demonstration setup was further optimized to obtain an improved output performance.

According to theoretical analysis, the proposed multi-stage system demonstrates higher exergy utilization efficiency. The subsequent numerical study reveals the significant influence of operating parameters such as heating temperature, supply water temperature, and mean pressure on the system's performance. Specifically, when the supply water temperature increases from 50 to 90 °C, the thermal-to-electric efficiency of the three-stage system decreases from 22.1% to 18.6%.

Theoretically, compared with a single-stage system, the exergy utilization efficiency improved from 36.3% to 43.9%, representing a relative improvement of more than 20%. In experiments, with an input heating power combination (21.8 kW for the first stage, 21.3 kW for the second stage, and 18.6 kW for the third stage), the demonstration setup provides a thermal power of 44.72 kW and an electric power of 10.18 kW simultaneously, resulting in an overall thermal-to-electric efficiency of 16.48% and an overall combined heat and power efficiency of 88.87%.

For a lower temperature ratio, the phase of the acoustic impedance at the output of the engine is approaching 90°. Preliminary optimization suggests that the thermal-to-electric efficiency of the three-stage system can be further improved to above 25%, and an even higher efficiency could be anticipated once a system-level optimization is conducted. Future research will focus on developing practical flue gas or combustion heating systems to facilitate the practical application of this technology.

RediT authorship contribution statement

Yuanhang Chen: Investigation, Software, Data analysis, Formal analysis, Writing- Original draft; **Guoyao Yu:** Funding acquisition, Conceptualization, Methodology, Writing - Review & Editing, Supervision; **Ying Ma:** Project administration, Investigation; **Jianhua Xue:** Investigation; **Fawad Ahmed:** Writing - Review & Editing; **Yangbin Cheng:** Investigation, Software; **Haojie Sun:** Investigation, Formal analysis; **Shunmin Zhu:** Investigation, Writing - Review & Editing; **Wei Dai:** Conceptualization, Methodology, Supervision; **Ercang Luo:** Funding acquisition, Conceptualization, Resources.

Acknowledgments

This work was financially supported by the National Natural Science Foundation of China (Grant No. 51876214) and the Special Research Assistant Project of the Chinese Academy of Science.

References

- [1] Mahmoudi A, Fazli M, Morad M R. A recent review of waste heat recovery by Organic Rankine Cycle. *Appl Therm Eng* 2018;143:660–75.
- [2] Jouhara H, Khordehghah N, Almahmoud S, et al. Waste heat recovery technologies and applications. *Therm Sci Eng Prog* 2018;6:268–89.
- [3] Johnson I, Choate WT, Davidson A. Waste heat recovery. Technology and opportunities in US industry. BCS, Inc., Laurel, MD (United States), 2008.
- [4] Hatami M, Ganji DD, Gorji-Bandpy M. A review of different heat exchangers designs for increasing the diesel exhaust waste heat recovery. *Renew Sustain Energy Rev* 2014;37:168–181.
- [5] Xu Z Y, Wang R Z, Yang C. Perspectives for low-temperature waste heat recovery. *Energy* 2019;176:1037–43.
- [6] Sprouse III C, Depcik C. Review of organic Rankine cycles for internal combustion engine exhaust waste heat recovery. *Appl Therm Eng* 2013;51(1–2):711–22.
- [7] Gou X, Xiao H, Yang S. Modeling, experimental study and optimization on low-temperature waste heat thermoelectric generator system. *Appl Energy* 2010;87(10):3131–6.
- [8] Jiang C, Zhu S, Yu G, et al. Numerical and experimental investigations on a regenerative static thermomagnetic generator for low-grade thermal energy recovery. *Appl Energy* 2022;311:118585.
- [9] Júnior E P B, Arrieta M D P, Arrieta F R P, et al. Assessment of a Kalina cycle for waste heat recovery in the cement industry. *Appl Therm Eng* 2019;147:421–37.
- [10] Haddad C, Périlhon C, Danlos A, et al. Some efficient solutions to recover low and medium waste heat: competitiveness of the thermoacoustic technology. *Energy Procedia* 2014;50:1056–69.
- [11] Zhu S, Yu G, Ma Y, Cheng Y, Wang Y, Yu S, et al. A free-piston Stirling generator integrated with a parabolic trough collector for thermal to electric conversion of solar energy. *Appl Energy* 2019;242:1248–1258.
- [12] Zhu S, Yu G, Liang K, Dai W, Luo E. A review of Stirling-engine-based combined heat and power technology. *Appl Energy* 2021;294:116965.
- [13] Zhu S, Wang K, González-Pino I, Song J, Yu G, Luo E, Markides CN. Techno-economic analysis of a combined heat and power system integrating hybrid photovoltaic-thermal collectors, a Stirling engine and energy storage. *Energy Convers Manage* 2023;284: 116968.
- [14] Jin T, Yang R, Wang Y, et al. Low temperature difference thermoacoustic prime mover with asymmetric multi-stage loop configuration. *Sci Rep* 2017; 7(1):1–8.
- [15] Yang R, Wang Y, Jin T, et al. Development of a three-stage looped thermoacoustic electric generator capable of utilizing heat source below 120 C. *Energy Convers Manage* 2018;155:161–8.
- [16] Keolian R. Truck thermoacoustic generator and chiller. Pennsylvania State Univ., University Park, PA (United States), 2011.
- [17] Li T, Tang D W, Li Z, et al. Development and test of a Stirling engine driven by waste gases for the micro-CHP system. *Appl Therm Eng* 2012;33:119–23.
- [18] Güven M, Bedir H, Anlaş G. Optimization and application of Stirling engine for waste heat recovery from a heavy-duty truck engine. *Energy Convers Manage* 2019;180:411–24.
- [19] Catapano F, Perozziello C, Vaglieco B M. Heat transfer of a Stirling engine for waste heat

- recovery application from internal combustion engines. *Appl Therm Eng* 2021;198:117492.
- [20] Catapano F, Frazzica A, Freni A, et al. Development and experimental testing of an integrated prototype based on Stirling, ORC and a latent thermal energy storage system for waste heat recovery in naval application. *Appl Energy* 2022;311: 118673.
- [21] Sahoo D, Kotrba A, Steiner T, et al. Waste heat recovery for light-duty truck application using thermoacoustic converter technology. *SAE Int J Engines* 2017;10(2):196-202.
- [22] Elferink M, Steiner T. Thermoacoustic waste heat recovery engine: Comparison of simulation and experiment. *Proc Mtgs Acoust* 2018; 35(1): 065002.
- [23] Mumith JA, Makatsoris C, Karayiannis TG. Design of a thermoacoustic heat engine for low temperature waste heat recovery in food manufacturing: A thermoacoustic device for heat recovery. *Appl Therm Eng* 2014;65(1–2):588–96.
- [24] Laazaar K, Boutammachte N. Development of a new technique of waste heat recovery in cement plants based on Stirling engine technology. *Appl Therm Eng* 2022;210:118316.
- [25] Alali AE, Al Khasawneh K. Performance analysis of stirling engine double-effect absorption chiller hybrid system for waste heat utilization from gas turbine modular helium reactor. *Energy Convers Manage* 2022;251:114976.
- [26] Nader W B, Chamoun J, Dumand C. Thermoacoustic engine as waste heat recovery system on extended range hybrid electric vehicles. *Energy Convers Manage* 2020;215:112912.
- [27] Li Q. Theoretical and Experimental Investigation on Multi-stage Thermoacoustic Heat Engine with Parallel Structure for Cascade Utilization of Variable Temperature Heat Sources. Ph.D thesis, University of Chinese Academy of Sciences;2018 [in Chinese].
- [28] Bi T, Wu Z, Zhang L, et al. Development of a 5 kW traveling-wave thermoacoustic electric generator. *Appl Energy* 2017;185:1355–61.
- [29] Luo E , Dai W , et al. Thermoacoustic engine system using temperature-change heat source: WO, WO2008131687 A1.
- [30] Qiu L, Wang B, Sun D, et al. A thermoacoustic engine capable of utilizing multi-temperature heat sources. *Energy Convers Manage* 2009;50(12):3187–92.
- [31] Francois M X, de Blok K, Bouakhao P, et al. The VALTA project: Full scale conversion of CHP engine flue gas heat into electricity. In: Proceedings of the 3rd international workshop on thermoacoustics, 2015.
- [32] Bi T. Theoretical and experimental study on acoustically-resonant double-acting travelling wave thermoacoustic electric generator. Ph.D thesis, University of Chinese Academy of Sciences;2017, p. 78–81 [in Chinese].
- [33] Backhaus S, Swift G W. A thermoacoustic Stirling heat engine. *Nature* 1999;399(6734):335–8.
- [34] Zhu S, Yu G, Jongmin O, et al. Modeling and experimental investigation of a free-piston Stirling engine-based micro-combined heat and power system. *Appl Energy* 2018;226:522–33.
- [35] Jiang Z, Xu J, Yu G, et al. A Stirling generator with multiple bypass expansion for variable-temperature waste heat recovery[J]. *Appl Energy*, 2023, 329: 120242.
- [36] White M, Qiu S, Wacknov J, et al. Conceptual design dssessment of megawatt-class multi-cylinder free-piston Stirling engines. in: 5th International Energy Conversion Engineering Conference and Exhibit (IECEC). 2007: 4703.
- [37] Wu Z, Yu G, Zhang L, et al. Development of a 3 kW double-acting thermoacoustic Stirling electric generator. *Appl Energy* 2014;136:866–72.
- [38] Yang H S, Zhu H Q, Xiao X Z. Comparison of the dynamic characteristics and performance of beta-type Stirling engines operating with different driving mechanisms[J]. *Energy*, 2023, 275: 127535.
- [39] Gedeon D. Sage user’s guide, Stirling, pulse-tube and low-T cooler model classes. 10th ed. Athens, OH: Gedeon Associates; 2014.

- [40] Zhu S, Yu G, Li X, et al. Acoustic field characteristics of a free-piston Stirling cryocooler with large cooling capacity at liquid nitrogen temperature. *Appl Therm Eng* 2019;147:324–35.
- [41] Xu J, Zhang L, Hu J, et al. An efficient looped multiple-stage thermoacoustically-driven cryocooler for liquefaction and recondensation of natural gas. *Energy* 2016; 101:427–33.
- [42] Wang H, Zhang L, Hu J, et al. Study on a novel looped heat-driven thermoacoustic refrigerator with direct-coupling configuration for room temperature cooling. *Int J Refrig* 2021;123:180–8.
- [43] Langdon-Arms S, Gschwendtner M, Neumaier M. A novel solar-powered liquid piston Stirling refrigerator. *Appl Energy* 2018;229:603–13.
- [44] Jiang Z, Yu G, Zhu S, et al. Advances on a free-piston Stirling engine-based micro-combined heat and power system. *Appl Therm Eng* 2022;217:119187.
- [45] Dai W, Luo E, Wang X, et al. Impedance match for Stirling type cryocoolers. *Cryogenics* 2011;51(4):168–72.



Citation on deposit: Chen, Y., Yu, G., Ma, Y., Xue, J., Ahmed, F., Cheng, Y., ...Luo, E. (2024). A thermally-coupled cascade free-piston Stirling engine-based cogeneration system. Applied Thermal Engineering, 236, Article

121679. <https://doi.org/10.1016...lthermaleng.2023.121679>

For final citation and metadata, visit Durham Research Online URL:

<https://durham-repository.worktribe.com/output/1930144>

Copyright statement: © 2023. This manuscript version is made available under the CC-BY-NC-ND 4.0

license <https://creativecommons.org/licenses/by-nc-nd/4.0/>